Molecular Nanoarchitectonic Sensing Layer for Analysis of Volatile Fatty Acids in Bioreactor Headspaces Using a Nanomechanical Sensor

Subrata Maji, Jan Hynek, Kazushi Nakada, Akiko Hori, Kosuke Minami, Jan Labuta, Mandeep K. Chahal, Daniel T. Payne, Gary J. Richards, Lok Kumar Shrestha, Katsuhiko Ariga, Yusuke Yamauchi, Genki Yoshikawa, and Jonathan P. Hill**

Anaerobic digestors (ADs) have the potential to become a major green energy source in a future sustainable society. To achieve this, effective operational parameters of the reactors must be established and maintained preferably by automation. In situ monitoring and control of AD systems is currently a challenging matter based on inconsistent feedstuff composition and the complexity of the biological processes involved, so that reactor shutdowns associated with costly downtime are a common problem. Here, a sensing device is developed for the monitoring of volatile fatty acids (VFAs), key intermediates during bioreactor operation, in the headspaces of anaerobic reactors. The device is compact, contains a sensing element based on a self-assembled molecular layer in conjunction with a nanomechanical sensor, and can be used to monitor VFA contents in bioreactors by estimating their relative contents in the reactor headspace in real time. This device allows the close monitoring of VFA concentrations in admixture toward cost-effective operation of bioreactors by reducing or eliminating reactor downtime. It represents a simple solution to the problem of real-time reactor monitoring, making anaerobic digesters a realistic alternative energy source.

1. Introduction

Anaerobic digestion (AD) has the potential to reduce greenhouse gas emissions by 15% and could produce 6–10% of global primary energy demand through biogas production. Worldwide, there are ≈132000 medium-to-large-scale digesters representing only 2% of the total estimated capacity of the AD industry.[1,2] AD is a complicated biological process involving various interacting microorganisms that degrade organic matter, including food waste, crop residues, animal manure, and sewage sludge, to produce biogas, bioplastics or organic fertilizers.[3–6] Effective and efficient production of biogas is only possible when all the biological processes (hydrolysis, acidogenesis, acetogenesis, and methanogenesis) at the digester

---

S. Maji, J. Hynek, J. Labuta, M. K. Chahal, D. T. Payne, L. K. Shrestha, K. Ariga, J. P. Hill
Research Center for Materials Nanoarchitectonics (MANA)
National Institute for Materials Science (NIMS)
1-1 Namiki, Tsukuba, Ibaraki 305-0044, Japan
E-mail: Maji.Subrata@nims.go.jp; Jonathan.Hill@nims.go.jp

K. Nakada, A. Hori, G. J. Richards
Department of Applied Chemistry
Graduate School of Engineering and Science
Shibaura Institute of Technology
Fukasaku 307, Minuma-ku, Saitama-shi, Saitama 337–8570, Japan

The ORCID identification number(s) for the author(s) of this article can be found under https://doi.org/10.1002/admt.202500294

DOI: 10.1002/admt.202500294

K. Minami, G. Yoshikawa
Research Center for Macromolecules and Biomaterials
National Institute for Materials Science (NIMS)
1-1 Namiki, Tsukuba, Ibaraki 305-0044, Japan

L. K. Shrestha
Department of Materials Science
Institute of Pure and Applied Sciences
University of Tsukuba
1-1-1, Tennodai, Tsukuba, Ibaraki 305–8573, Japan

K. Ariga
Department of Advanced Materials Science
Graduate School of Frontier Sciences
The University of Tokyo
5-1-5 Kashiwanoha, Kashiwa, Chiba 277–8561, Japan

Y. Yamauchi
Department of Materials Process Engineering
Graduate School of Engineering
Nagoya University
Nagoya 464–8603, Japan

Y. Yamauchi
Australian Institute for Bioengineering and Nanotechnology (AIBN) and
School of Chemical Engineering
The University of Queensland
Brisbane, QLD 4072, Australia

interior operate smoothly. If one of these processes is inhibited or arrested, then there is an immediate impact on the other processes, which leads to losses in production or necessitates shutdown of the plant.[7–10] Organic overload, where the volume of organic matter fed to the digester exceeds the degradation capacity of the microorganism, is a common problem in AD.[11–13] In that case, organic matter is only partially degraded to volatile fatty acids (VFAs; acetic, propionic, butyric acids), which then accumulate inside the reactor, causing digester acidification. Therefore, the concentrations of individual VFAs at digester interiors must be monitored to establish process stability by controlling feedstock composition and to understand the interaction and inhibition of different groups of microorganisms in the reactor.[14–17] A moderate accumulation of acetic acid in the digester is normal, as acetic acid is the final precursor to methane. However, the accumulation of the longer chain fatty acids (propionic acid, butyric acid) indicates severe process instability, which may lead to reduced biogas production or plant failure. Therefore, the monitoring of acetic acid, propionic acid, and butyric acid levels in the digester is very important to follow the biogas production. It should also be noted here that other types of AD based on different microorganisms (e.g., propionic acid bacteria) operate under high levels of propionic acid[18] or butyric acid,[19] and monitoring of their levels remains critical in both cases. High-performance liquid chromatography (HPLC), gas chromatography (GC), or GC-mass spectrometry (MS) are used to monitor individual VFAs.[20–22] These offline laboratory-based techniques are expensive, time-consuming, and require expert operation to obtain reliable results. Therefore, it would be highly beneficial to develop high-performance VFA sensors for the simultaneous detection and discrimination of VFAs in the digester for remote real-time sensing and interfacing with Internet of Things (IoT) based technologies, toward the automation of the biogas plant. To date, there are relatively few reports of vapor sensors for VFAs, including those for acetic acid (for recent examples see A. Akhtar et al.[23] and N. J. Pineau et al.[24]), propionic acid,[25,26] and butyric acid.[27] These are largely based on inorganic nanomaterials[28–31] in different sensing devices, including quartz crystal microbalance[32,33] or electronic nose configurations.[34,35] Other examples have relied on a metal-organic-framework (MOF) component[36] or other receptor films[37,38] for operation, and bioelectrochemical methods are known.[39] A comparison of the available performance metrics of selected sensors is shown in Table S1 (Supporting Information). Reports of simultaneous VFA monitoring are also rare[40–42] mostly involving mixtures of acetic and propionic acids, although monitoring of more complex mixtures has also been investigated.[43,44] Finally, while interference from other analytes can be a serious drawback in sensing operations,[45] in the case of VFAs, oligomerization of the carboxylic acid analytes is a specific interaction[46] that is difficult to account for since little is known about the dynamics of that interaction in vapor mixtures.

Nanomechanical sensors present a promising gas or vapor monitoring technology based on their high sensitivity, miniature size, and low power consumption.[47–49] These sensors can be used to detect mechanical changes caused by the interaction of a selective receptor layer (adhered at the sensor active surface) with targeted analytes. For example, the Membrane-Type Surface stress Sensor (MSS) is an advanced, optimized nanomechanical sensor exhibiting excellent sensitivity due to its unique structure, which consists of a silicon membrane embedded with four piezoresistors sensing beams in a Wheatstone bridge-type configuration to maximize the output signal.[50–53] Receptor-layer-coated MSS generates adsorption-induced surface stress at the silicon membrane in the presence of targeted analytes, especially those in the vapor phase, and the resulting surface stress is transduced through the four piezoresistors sensing beams, which generate sensing responses. In principle, any kind of material can be used as a receptor layer for MSS, including polymers, nanomaterials or small organic molecules, but they must exhibit mechanical deformation caused by interactions with the analyte. The receptor layer material, regardless of its identity, must also be attached firmly to the MSS silicon membrane in order that adsorption of the analyte induces sufficient mechanical deformation of the receptor layer in turn generating maximum stress at the silicon membrane. In the case of AD process monitoring, other parameters, including selectivity for VFAs and low sensitivity to water, are both critical for the implementation of MSS to monitor real-time acid concentrations. We have demonstrated the measurements of VFAs in silage samples for their quality evaluation using common polymers as receptor materials coated on MSS,[54] while advanced functional materials with higher performance are anticipated for practical on-site monitoring in AD. Recently, we have developed porphyrin-based coordination complexes whose unique structures allow for solution-based casting of porous architectures onto the MSS membrane by using inkjet printing.[55] These unique materials have large specific surface areas available for gas or vapor adsorption and are capable of generating very high strain at the MSS surface, leading to large sensing responses. These materials also show robust performance under conditions of high humidity (>90% RH), a critical property in biological process monitoring applications, and they can also be modified using organic synthesis techniques.

In this work, we demonstrate the dynamic analysis of different volatile fatty acids in the vapor phase at sub-ppm sensitivity under high relative humidity conditions. For this purpose, we introduce an advanced 2nd generation porphyrin receptor layer referred to as ***β*-NiOx1**, which forms a nanoporous polycrystalline film when deposited on the MSS sensor chip and shows excellent selectivity toward volatile fatty acid vapors. Importantly, the ***β*-NiOx1**@MSS hybrid device can be used to analyze mixtures of low concentration VFA vapors in the high humidity regime (>90% RH) due its general low response to humidity as an interfering agent.[56] This device ***β*-NiOx1**@MSS allows the close monitoring of volatile fatty acid concentrations in admixture toward cost-effective operation of bioreactors by reducing or

Y. Yamauchi
Department of Chemical and Biomolecular Engineering
Yonsei University
50 Yonsei-ro, Seodaemun-gu, Seoul 03722, South Korea

G. Yoshikawa
Materials Science and Engineering
Graduate School of Pure and Applied Science
University of Tsukuba
1-1-1 Tennodai, Tsukuba, Ibaraki 305–8571, Japan

eliminating reactor downtime. Overall, this **β-NiOx1** receptor material, used in conjunction with MSS, is the most important development so far to address the critical challenge of full automation of biogas plants. Such solution processable porous receptor materials are highly suitable for applications involving nanomechanical sensors for monitoring different targeted VOCs.

2. Results

The porphyrin[57] molecules used in this work are known by the general term **NiOx**, and are available in 1st generation and now a more advanced 2nd generation of compound ("**α**" and "**β**", resp.). Each **NiOx** compound can be obtained in two different oxidation states ("**Ox1**" and "**Ox3**"). For example, the most effective 1st generation material is **α-NiOx3,** based on its high specific surface area and the high sensitivity and selectivity of the resulting **α-NiOx3**@MSS hybrid sensors to acetone under high humidity (see M. K. Chahal et al.[55] for the structure of **α-NiOx3**). Here, we have developed the 2nd generation **β-NiOx1** (see **Figure** 1a for the structure of **β-NiOx1** and its direct precursor; see Supporting Information for details of their synthesis).

In contrast to 1st generation **α-NiOx1**, which has a small specific surface area (for 1st gen. materials, **α-NiOx3** has a large surface area), **β-NiOx1** exhibits microporosity in its as-isolated powder state, it is highly soluble in different organic solvents (**β-NiOx3** has a low specific surface area), and provides microporous solids on evaporation of its solutions. Thus, **β-NiOx1** can be considered a "smart" building block for sensor nanoarchitectonics[58] by in situ synthesis of porous monoliths. For example, inkjet deposition of this material onto an MSS sensing chip (Figure 1b,c) yields a receptor layer film composed of a porous polycrystalline sheet network (Figure 1d,e), with an average thickness of 60 nm. Such a porous polycrystalline sheet attached with a sensor platform can be used to detect volatile organic compounds (VOCs), especially targeted VFAs, with strong specific interaction.

In order to assess the possibility of using the **β-NiOx** materials as MSS receptor layers, their specific surface areas (SSA) were estimated by determining their nitrogen adsorption-desorption isotherms (surface area is a critical parameter, often a determining factor in the sensing efficacy of MSS receptor layer materials). N_2 adsorption isotherms of **β-NiOx1** (and **β-NiOx3**) are shown in Figure 1f revealing that, while it appears to possess a microporous structure, **β-NiOx3** has a much smaller surface area (123 $m^2\ g^{-1}$) than **β-NiOx1** (670 $m^2\ g^{-1}$), which also exhibits microporosity with a Type III hysteresis loop indicating the copresence of meso- and micropores. Additionally, the presence of the hysteresis loop indicates the formation of plate-like structures, which can be seen in SEM images (Figure 1d,e). The pore size data for **β-NiOx1** (Figure 1g,h) indicate a narrow distribution dominated by micropores with nanometric pore diameters. These data (and SEM images; see Figure 1d,e) establish that **β-NiOx1** is a strong candidate for application as an MSS receptor layer based on its highly porous interleaved polycrystalline structure. Porous receptor materials with uniform pore size and high surface area can produce a high level of sensitivity when incorporated in multicomponent gas/vapor sensor devices.

In order to determine the origin of its microporous structure, single crystals of **β-NiOx1** were grown by slow diffusion of methanol into a chloroform solution of the compound. The single crystal X-ray structure is shown in **Figure** 2. Figure 2a shows the molecular structure with an extended π electronic surface due to the fused benzimidazole component (see also Figures S1 and S2, Supporting Information).

Peripheral meso-substituents are not coplanar with the conjugated core except where fused (Figure 2b; see caption for details), and the conjugated surface of the molecule is slightly curved, probably to maintain the coordination to Ni(II). Molecules form a dimer unit in the crystals (Figure 2c; Figure S3, Supporting Information) involving several supramolecular interactions especially C═O...H—C hydrogen bonding, C—H...Br—C H—bonding, and C—H...N H—bonding. Dimer units pack to form a porous structure (Figure 2d; Figure S4, Supporting Information) where voids in the crystal are initially occupied by chloroform molecules of solvation, none of which contribute to the structure. Note that methyl and 4-bromophenyl substituents protruding into the channels are mutually remote so that voids running through the crystal are continuous parallel to the a-axis (Figure 2e). Interestingly, the multiple supramolecular interactions operating in crystals of **β-NiOx1** are sufficiently strong to maintain its structure in the absence of solvent so that it exhibit a large SSA (Figure 1g) even after annealing at 120 °C. This is similar to the case for **α-NiOx3**, whose crystal structure could be remeasured even after solvent evacuation[55] and other porous structures such as hydrogen-bonded organic frameworks (HOFs).[59,60] Chloroform contained in the channels is present as chains of solvent, which are non-structural in nature. Chains are maintained by C—H...Cl hydrogen bonding and Cl...Cl interactions (Figure S5a,b; Supporting Information). An additional smaller pore is present orthogonal to the main pore (Figure 2f).

β-NiOx1 can be inkjet printed on MSS membrane surfaces (for SEM morphology see Figure S6, Supporting Information), giving **β-NiOx1**@MSS, which was tested using the experimental set-up shown in **Figure** 3a. Figure 3b shows a survey of the sensing responses of **β-NiOx1**@MSS in the presence of water and three major volatile acids: acetic acid, propionic acid, and butyric acid vapors. Importantly, **β-NiOx1** shows excellent sensitivity toward vapors of each of the acids, with the highest sensitivity to acetic acid. Additionally, **β-NiOx1** shows the lowest sensitivity and selectivity to water vapor, which is a significant advantage for real-time applications of this receptor material. In contrast, **β-NiOx3** with a lower surface area (123 $m^2\ g^{-1}$) shows much weaker sensing responses (up to several orders of magnitude weaker), most likely due to its lower adsorption capacity for the different VOCs (Figure 3c). This contrasts with the 1st generation materials **α-NiOx1**/**α-NiOx3** (previously referred to as **1** and **1-ox**, resp.)[55] where the higher oxidation state **α-NiOx3** material possesses a significantly larger specific surface area (475 $m^2\ g^{-1}$ versus 15 $m^2\ g^{-1}$ for **α-NiOx1**) with excellent selectivity to acetone and alcohol vapors.

Based on the speculation that selectivity might be tuned by varying molecular structure in the **α-NiOx1** system, we sought a receptor sensitive to vapor phase VFAs, because there is a general dearth of materials suitable for this purpose.[61] By making simple modifications of the functional group in **α-NiOx1**[55] to prepare **β-NiOx1**, we have successfully varied the sensitivity of the materials from acetone to volatile fatty acids. It was gratifying to note that **β-NiOx1**@MSS hybrid sensor shows intense,

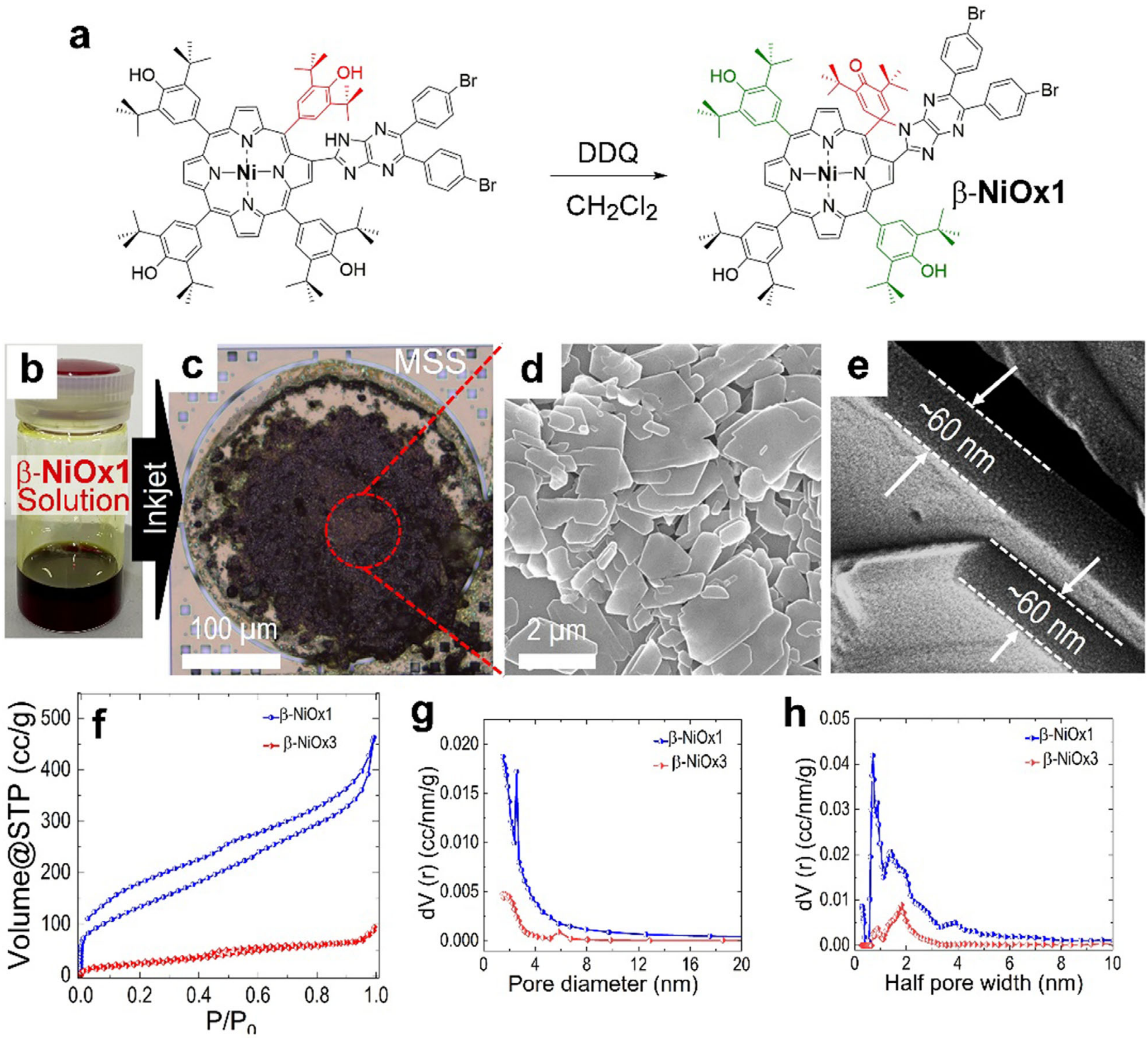

Figure 1. Synthesis and textural properties of polycrystalline nanoporous receptor material and interfacial layer for nanomechanical sensing devices (MSS). a) Synthesis of **β-NiOx1** (see also Scheme S1, Supporting Information): treatment of the precursor with 2,3-dichloro-5,6-dicyano-1,4-benzoquinone (DDQ) in dichloromethane. b) corresponding solution of **β-NiOx1** in toluene. Film formed by inkjet deposition on MSS sensor chip using **β-NiOx1** dissolved in DMF. c) Optical micrograph of receptor material **β-NiOx1** inkjet-printed onto MSS sensor device. d) SEM morphology of **β-NiOx1** film shows interleaved polycrystalline sheets. e) Edge-view SEM image of **β-NiOx1** crystalline sheet indicates uniformly thin (≈60 nm) crystallites. f) Nitrogen adsorption isotherms for **β-NiOx1** (and **β-NiOx3**) obtained following sample annealing at 120 °C for 24 h. g) Pore size distribution profile obtained by using the density functional theory (DFT) method. h) Pore size distribution profile obtained by the Barrett—Joyner–Halenda (BJH) method.

rapid responses in the presence of acetic, propionic, and butyric acid vapors, and the responses are 4–6-fold greater than that to water vapor. The relative intensity of the different acid responses (Figure 3b) decreases with increasing molecular weight as expected due to their relative saturated vapor pressures (acetic acid: 20.9 mmHg; propionic acid: 3.3 mmHg; butyric acid: 1.65 mmHg at 25 °C), which control their concentrations in the gas phase. Time-dependent adsorption-desorption kinetics play an important role to understand the interaction of different vapors with the porous receptor material. The adsorption-desorption-induced MSS signals can be fitted with the double-exponential (DE) model, which assumes that there are two kinetic barriers for the adsorption of VFAs into the porous receptor materials.[62,63] The first kinetic barrier is due to the diffusion through the window of the porous framework or outer layer of the receptor layer, which is the faster process. The second barrier is due to the diffusion through the pore cavities, which is the slower process and depends solely on the receptor material identity. The DE curve fitting model is given by the following Equation (1):

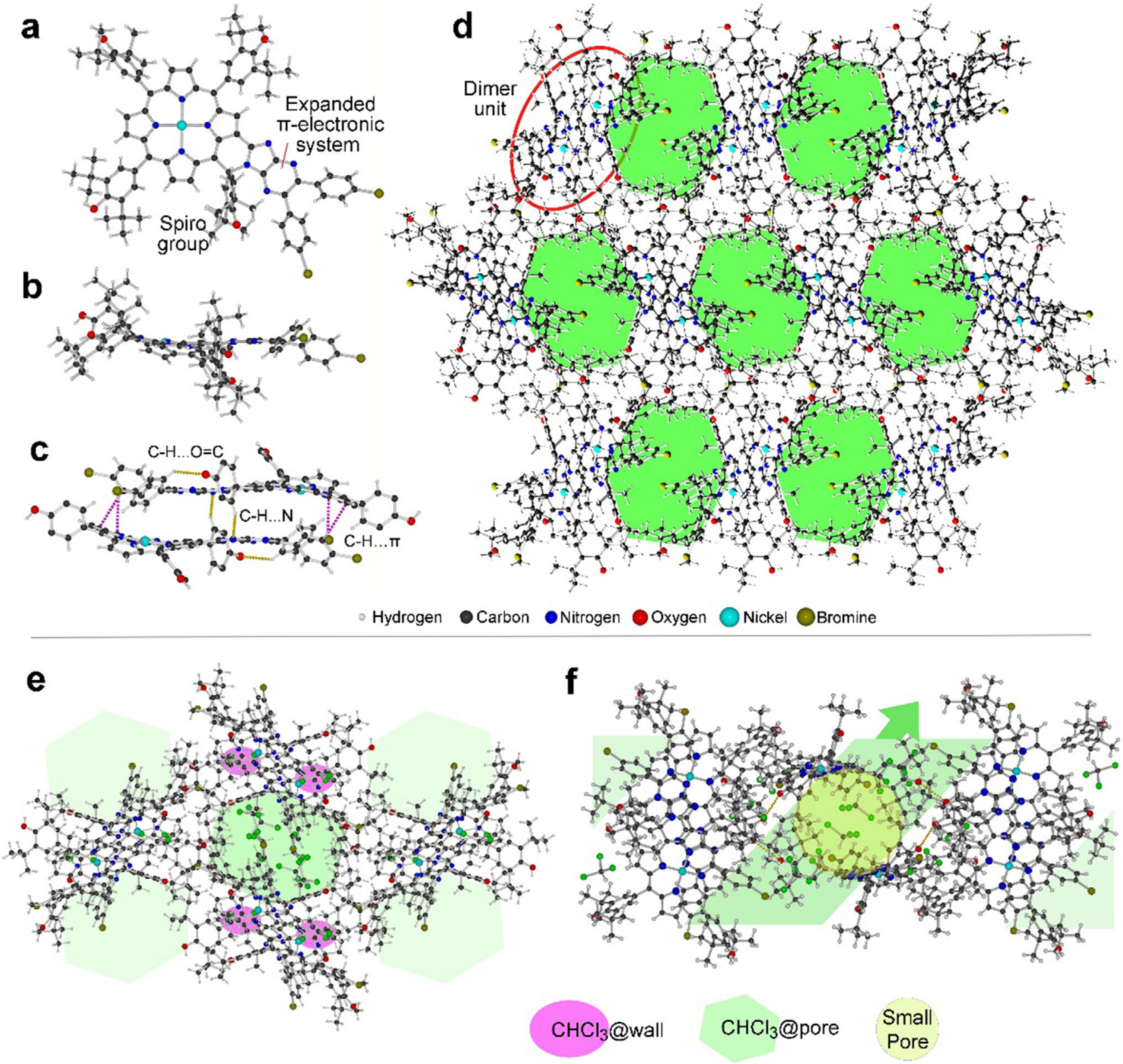

Figure 2. X-ray crystal structure of ***β*-NiOx1**. a) Molecular structure showing the extension of the π-electronic system by fusion at a bay area (Bond lengths and angles: Ni-N$_{av}$: 1.94 Å; C-Br: 1.89 Å; spiro—C═O: 1.22 Å; phenol C—O: ≈1.37 Å). b) Edge view of the molecule showing the slight "S"-shape (Dihedral angles with average porphyrin plane: 4-BrPh: 48.2°, 43.5°; phenols (clockwise from fused groups): 44.1°, 48.8°. c) Dimer structure of ***β*-NiOx1** with important interactions highlighted (Interaction lengths and angles: spiro-C═O…H—C: 2.74 Å; C—H$_{ar}$…N: 2.66 Å; C—H…π: 2.76, 2.77 Å. For more information, see Figure S3, Supporting Information). d) Packing structure of ***β*-NiOx1** viewed along the a-axis showing solvent-filled voids highlighted in green. The red ellipse identifies a single dimer unit. (See also Figures S1–S5, Supporting Information). e,f) Pore structures containing chloroform molecules in ***β*-NiOx1**. e) Main pore viewed parallel to the a-axis. f) Minor pore (yellow circle) viewed perpendicular to the main pore channel. The green arrow denotes the direction of the a-axis. Green shading denotes the main pore; pink ellipses in (e) indicate $CHCl_3$ bound close to the pore wall.

$$\frac{M_t}{M_e} = A_1\left(1 - e^{-k_1 t}\right) + A_2\left(1 - e^{-k_2 t}\right) \tag{1}$$

where M_t is the mass uptake at time t and M_e is the equilibrium mass uptake, k_1 and k_2 represent the kinetic rate constants ($k_1 > k_2$). A_1 and A_2 are the relative contributions of the two energetic barriers controlling the adsorption process, with $A_1 + A_2 = 1$. In the case of MSS, the mass uptake is directly proportional to the strain and the corresponding output voltage.[64] Therefore, the above equation can be further correlated with the MSS signals as Equation (2):

$$\frac{V_t}{V_e} = A_1\left(1 - e^{-k_1 t}\right) + A_2\left(1 - e^{-k_2 t}\right) \tag{2}$$

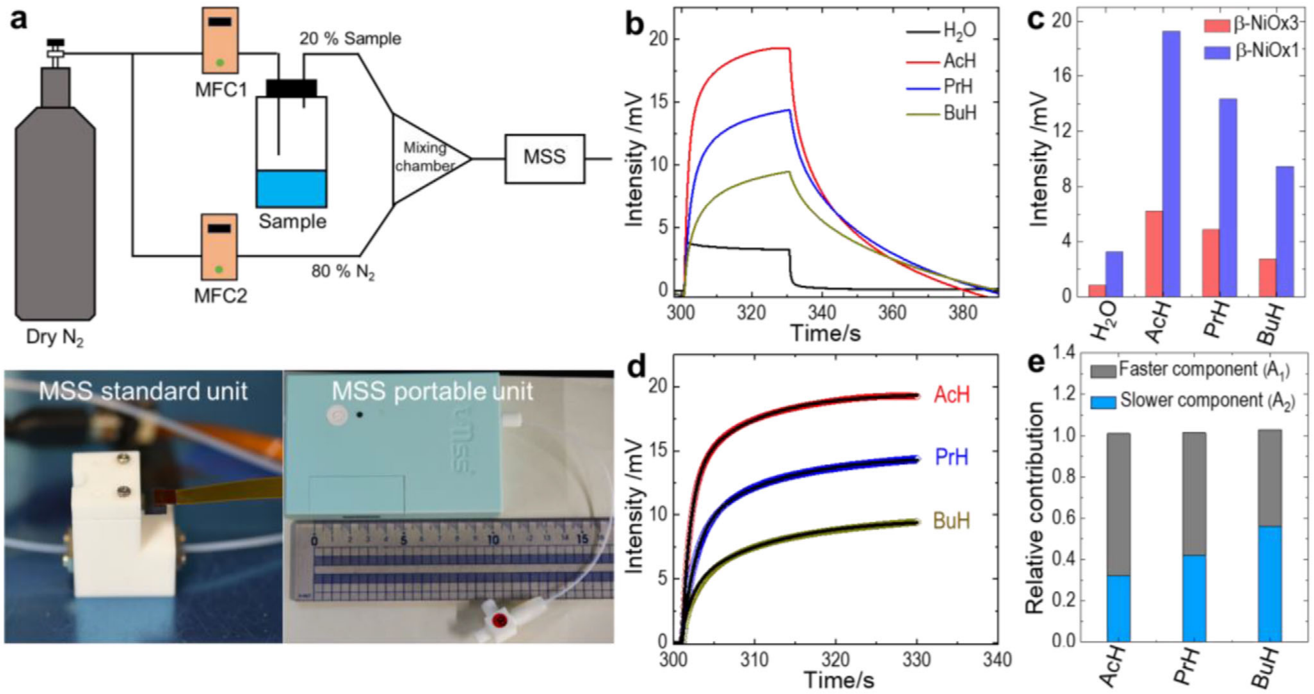

Figure 3. MSS sensing using ***β*-NiOx1**. a) Schematic showing MSS vapor measurement setup including standard and portable MSS unit. b) MSS response of ***β*-NiOx1**@MSS in the presence of water vapor and VFAs: acetic acid (AcH), propionic acid (PrH), and butyric acid (BuH). c) Relative sensitivities of highly porous ***β*-NiOx1**@MSS and low porosity ***β*-NiOx3**@MSS (see also Figure S7, Supporting Information). d) Adsorption kinetics of different VFAs (AcH, PrH, and BuH) by the receptor material ***β*-NiOx1**. e) The relative contribution of the slower and faster components for the different acids.

The desorption process can also be modeled as a similar two-stage process using the following Equation (3):

$$\frac{V_e}{V_t} = A_1 \left(e^{-k_1 t}\right) + A_2 \left(e^{-k_2 t}\right) \qquad (3)$$

where V_t is the output voltage at time t and V_e is the equilibrium output voltage. Figure 3d shows the well-fitted adsorption curves based on Equation 2 with a regression coefficient $R^2 > 99\%$. Figure 3e shows the relative contribution of fast and slow diffusion processes at the receptor material interior for the three acids. Here we can see that the contribution from the slower process (diffusion inside the pore cavity) increases from acetic to butyric acid. This increase in the slower component can be attributed to the slower diffusion of butyric acid and propionic acid inside the pore cavity of the ***β*-NiOx1** receptor material relative to acetic acid. As a result, at a fixed time, the quantities of acid adsorbed inside the receptor material follow the order: acetic acid > propionic acid > butyric acid, which is exactly similar to the MSS sensitivity (Figure 3b). The differences in the diffusion process for different VFAs are critically important for their discrimination in complex mixtures and might allow for their analysis by the MSS hybrid sensor without the requirement for sophisticated machine learning techniques or other expensive devices. Fitting of desorption processes of MSS signals also shows a similar trend for different VFAs as shown in Figure S8 (Supporting Information). Desorption processes are increasingly dominated by the slower component, which can be attributed to the slower desorption process from the pore cavity.

Previous studies indicate that different VFAs form during the acidogenesis process occurring in AD plants, with acetic acid being the dominant intermediate, accounting for more than 75% of AD methane production.[65,66] Propionic and butyric acids are of secondary importance, being eventually converted to acetic acid and hydrogen.[67,68] Analysis suggests that the total VFA concentration should be in the range of 1000–4300 mg L^{-1} (≈15–100 mM) to maintain process stability of biogas plants. While the individual fatty acids concentration may vary, the total concentration should lie in this range for stable reactor operation, and slightly acidic to neutral pH 5.5–7.0 is optimum for VFA production/conversion inside the biogas plant. VFAs are polar molecules forming strong hydrogen bonds with water, making their analysis in vapor or gas phase at reactor interiors a challenging task. To simulate biogas plant conditions, we prepared different solutions of acetic acid, propionic acid, and butyric acid in water in the operating concentration range. Proton-transfer reaction mass spectrometry (PTR-MS) was used to determine the headspace concentrations over the acid solutions, leading to vapor phase acid concentrations in the sub-ppm (0.45 ppm) to tens of ppm (70 ppm) range for all the acids, depending on their concentrations in solution (Table S3, Supporting Information). The headspaces are also saturated with water vapor (RH = 100%), simulating the expected condition at the interiors of AD reactors of biogas plants so that the receptor material is required also to be relatively insensitive toward water vapor. The ***β*-NiOx1**@MSS shows excellent performance for the detection

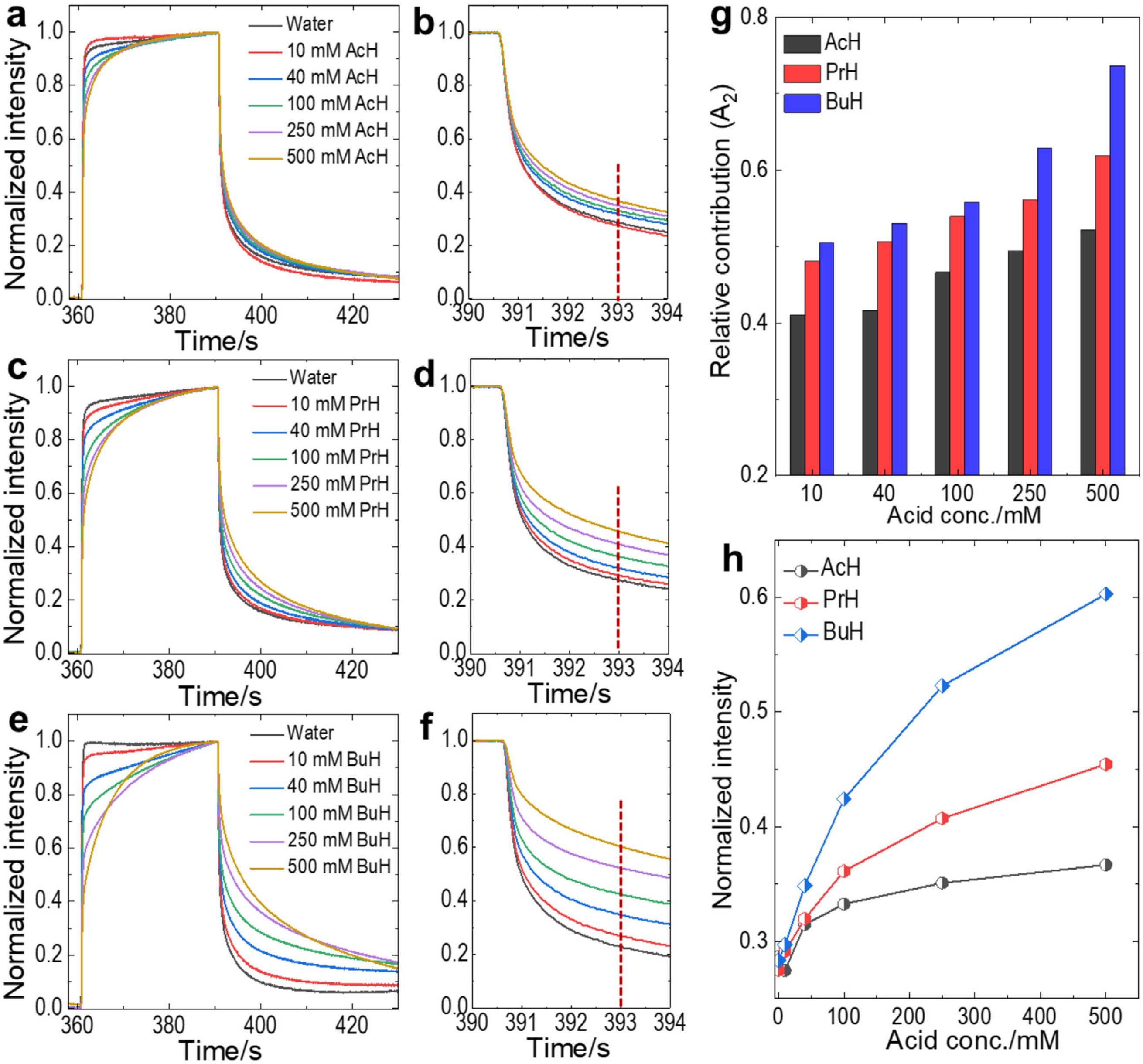

Figure 4. Sensing response of ***β*-NiOx1**@MSS in headspace analysis over different concentrated (0-500 mM) VFA solutions in water. a) Sensing response of acetic acid (AcH) solution with magnified desorption curve (b). c) Sensing response of propionic acid (PrH) solution with magnified desorption curve (d). e) Sensing response of butyric acid (BuH) solution with magnified desorption curve (f). The red dashed line in all the magnified desorption curves indicates the selected point to construct the calibration plot. g) Relative contribution of the slower components in the desorption curves for the different acid solutions. h) Plot of MSS desorption intensity (393 s) versus solution concentration for calibration of headspace acid concentration of aqueous solution.

of different VFAs in the headspaces of the low-concentration solutions in water, as shown in **Figure** 4. Typical sensing responses of ***β*-NiOx1**@MSS to acetic acid (AcH) (Figure 4a,b), propionic acid (PrH) (Figure 4c,d), and butyric acid (BuH) (Figure 4e,f) vapors reveal the clear discrimination of low-concentration acid solutions even at sub-ppm headspace acid concentration. All the signal profiles differ from that of pristine water vapor and follow adsorption-desorption profiles similar to pure acid, even under these high-humidity conditions. Sensing responses (adsorption and desorption curves) of individual VFAs (AcH, PrH, and BuH) differ and also follow similar trends of desorption of the pure acids (Figure S8, Supporting Information) and can be used to differentiate the responses at different concentrations. Signal profiles obtained over acetic acid solution (Figure 4a,b) show fast adsorption and desorption due to its low molecular weight and high vapor pressure, which induce fast diffusion inside the pore cavity of the receptor layer. In contrast, response over butyric acid solutions (Figure 4e,f) shows the slowest adsorption/desorption characteristics due to its relatively low vapor pressure and large size, which leads to slow diffusion in the receptor material.

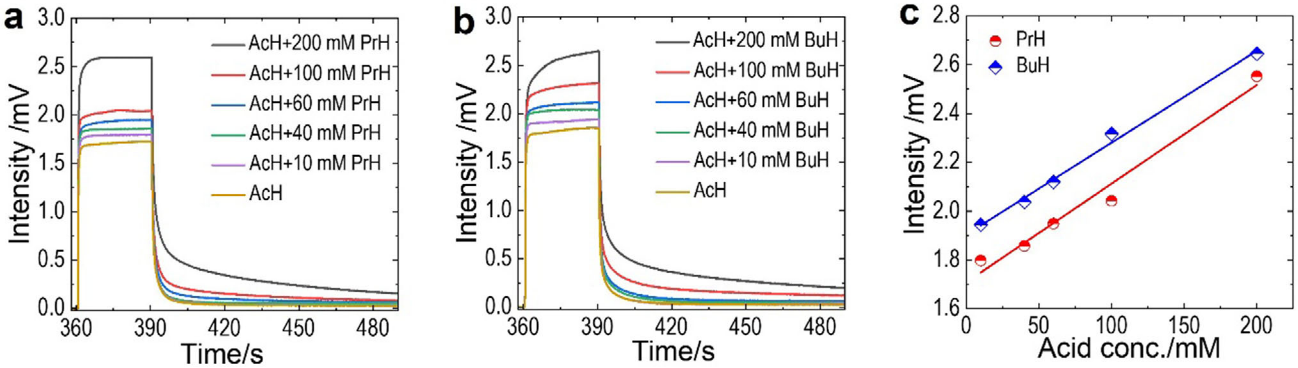

Figure 5. Calibration of **β-NiOx1**@MSS response over aqueous solutions of binary acid mixtures (i.e., a ternary mixture, two acids plus water). a) Sensing response to headspace vapors over different mixtures with fixed acetic acid (AcH) and variable propionic acid (PrH) concentration (10–200 mM) at room temperature (25 °C). b) Sensing response to headspace vapors over different mixtures of fixed acetic acid (AcH) and variable butyric acid (BuH) concentration (10-200 mM) at room temperature (25 °C). c) Plot near saturation MSS intensity (390 s) versus propionic or butyric acid concentration to monitor any abrupt change in propionic or butyric acid level.

Fitting of the desorption curves of individual acids (Figure S9, Supporting Information) clearly indicates that the desorption is dominated by slow desorption from the pore cavity of the **β-NiOx1** receptor material. Figure 4g shows the relative contribution of slow desorption of the different VFAs from the porous receptor material. On average, 40–70% of the total decay curve is dominated by slow desorption of the acids, and the rate of decay depends on the individual acids. Therefore, differences in desorption intensity at fixed time have been used to calibrate the relationship between desorption intensity and acid concentration. Here, desorption intensity at 393 s has been selected arbitrarily to quantify the acid concentration in the headspace vapor over solutions of the individual acids. Desorption at this point is dominated by slow desorption from the pore cavity, which is directly related to the receptor layer property. Figure 4h shows the variation of desorption intensity at 393 s (i.e., 3 s after N_2 injection) at different acid concentrations. There is a nonlinear correlation between acid concentration and MSS desorption intensity for individual acids. At low concentration (0–100 mM), the variation follows almost linear correlation with evidence of saturation at higher concentration (>100 mM). Saturation at higher concentrations can be attributed to MSS signal saturation due to excessive acid vapor concentration. Intensity calibration curves shown in Figure 4h can be used to clearly differentiate the acids at low concentrations even under high humidity conditions, which is a significant development toward continuous VFA monitoring in biogas plants. For purposes of comparison, the response of the 1st generation receptor layer **α-NiOx3**@MSS was also measured (Figure S10, Supporting Information), revealing that **α-NiOx3** can also be used to analyze the concentration of butyric acid by headspace analysis. However, the performance of **α-NiOx3**@MSS is poor compared to **β-NiOx1**@MSS (see Figure S10c, Supporting Information), illustrating the importance of molecular structure and thus crystal morphology in the excellent selectivity of **β-NiOx1** toward VFAs.

The possibility of using the **β-NiOx1** receptor material to differentiate propionic acid or butyric acid from acetic acid in aqueous mixtures similar to those encountered in AD reactors was also investigated. Basically, the concentrations of propionic acid and butyric acid are important determinants of AD process imbalance and indicators for AD plant shutdown. Therefore, the monitoring of these acids in the presence of acetic acid while challenging is also a critical matter. Solutions containing a fixed concentration of acetic acid (40 mM) with a range of propionic and butyric acid concentrations (10–200 mM) were prepared in water, and the headspace vapor of the acid mixture was monitored using **β-NiOx1**@MSS.

Figure 5a shows the sensing responses of the mixed acid samples of 40 mM acetic acid with varied concentrations of propionic acid, illustrating the capability to differentiate propionic acid from acetic acid in aqueous mixtures by using receptor material **β-NiOx1**. Small variations in propionic acid concentration in the aqueous binary mixtures (i.e., a ternary mixture with water effectively being eliminated by its rapid desorption) are reflected in the **β-NiOx1**@MSS sensing responses. Saturated intensity of the MSS signal increases with propionic acid concentration as can be seen from Figure 5a. Similarly, variation of butyric acid concentration can be easily differentiated from acetic acid at fixed concentration in aqueous mixture by using the **β-NiOx1**@MSS responses as shown in Figure 5b. Nearly saturated intensity of **β-NiOx1**@MSS signals has been used to correlate the variation in propionic and butyric acid concentrations in headspace with fixed acetic acid concentration in the mixture. Figure 5c shows the correlation between MSS-saturated intensity with propionic and butyric acid concentrations (10–200 mM). It is indispensable to construct such calibration curves for monitoring of the real-time variation of propionic or butyric acid concentrations and maintaining stable AD plant operation. By calibrating the headspace analysis, any sudden increases in propionic or butyric acid concentrations in the reactor can be detected in real-time simply by using the **β-NiOx1**@MSS sensor signal. These characteristics of the **β-NiOx1**@MSS device make it highly suitable for continuous monitoring of VFAs in biogas plants to maintain reactor stability and improve the efficiency of AD processes to establish carbon-sustainable processes.

3. Discussion and Conclusion

Adsorption/desorption processes lead to high sensitivities for these porous receptor materials and depend strongly on their solution processability, where in situ crystallization and adhesion on the sensor platform result in an effective porous material-sensor interface. Most of the known porous receptor materials form poor quality films, which are incompatible with sensing applications and exhibit low sensitivity and selectivity. In contrast, compound **β-NiOx1** is a microcrystalline powder with a highly porous structure and is readily soluble in common organic solvents to form a clear solution as shown in Figure 1b. Upon inkjet deposition on MSS (Figure 1c), **β-NiOx1** forms a uniform interleaved polycrystalline network film, as shown in Figure 1d,e. SEM analysis of this inkjet film shows the formation of supramolecular sheets on the MSS membrane, where cross-sectional analysis of the supramolecular sheet using SEM shows a uniform thickness of the crystal components of ≈60 nm (Figure 3f). **β-NiOx1** also exhibits a similar sheet-like morphology by solution drop-casting (Figure S6a,b, Supporting Information). Additionally, the sheet formation of **β-NiOx1** on MSS membrane is not affected by inkjet droplet number (Figure S6c–h, Supporting Information), which indicates the advantages associated with the novel solution-processable **β-NiOx1** receptor material. Finally, sensor stability is an important factor, especially in applications involving potentially corrosive analytes or where continuous monitoring is expected. This issue has been addressed by exposing the sensor to a fixed concentration of acetic acid (40 mM in water) in humid air, involving a repeated exposure-readout-desorption mode for 2000 cycles. Figure S11a,b (Supporting Information) shows the change in intensity with cycle number. The **β-NiOx1**@MSS sensor shows extended cycle life with 85% retention of initial intensity even after 2000 cycles, which confirms that **β-NiOx1** is an excellent receptor material for VFA sensing. Also, we have confirmed that sensor devices are stable under storage in the dark for periods beyond 2 years indicating excellent possible shelf-lives of the **β-NiOx1**@MSS sensor devices (see Figure S11c,d, Supporting Information).

In summary, the receptor material **β-NiOx1** can be used in conjunction with MSS nanomechanical sensor technology (as the **β-NiOx1**@MSS sensor device) for the estimation of low molecular weight volatile fatty acids (VFAs) in admixture at high relative humidity at the low concentrations suitable for monitoring of AD reactor biogas plants. This work thus obviates the existing requirement of expensive equipment or time-consuming laboratory testing for monitoring the acid concentration making it possible to replace those with an inexpensive, disposable (or reusable) chip sensor used in conjunction with a mobile device. The substantial differentiation of analytes at low concentration in aqueous media (here in the vapor phase) represents a milestone for sensing technologies aimed at monitoring and diagnosis since it is possible not only to adapt the technology from the molecular level up to customize the sensor response to particular analytes but also to employ machine learning techniques to parse data for the estimation of the compositions of complex mixtures. In the case described here, monitoring of AD reactors can be used to optimize reaction conditions and also to prevent costly reactor downtime toward an efficient carbon sustainable society. Additionally, we note that the presence and composition of VFAs contained in the human gut biome are an important factor in determining general digestive health[69] but also affect several disease states,[70] including cancer,[71] and has even been reported to affect cognitive function[72] further improving the prospects of technologies aimed at monitoring VFAs in situ or batch analyses. We are currently investigating how the present system might be adopted for this purpose.

4. Experimental Section

General Experimental: Reagents and dehydrated solvents (in septum-sealed bottles) used for syntheses and spectroscopic measurements were obtained from Tokyo Kasei Chemical Co., Wako Chemical Co., or Aldrich Chemical Co. and were used without further purification. Electronic absorption spectra were measured using a JASCO V-570 UV/Vis/NIR spectrophotometer or a Princeton Applied Research (PAR) diode array rapid scanning spectrometer. ATR-FTIR spectra were obtained using a Thermo-Nicolet 760X FTIR spectrophotometer equipped with a SMART-iTX ATR accessory. Electron spin resonance (ESR) spectra were measured from solid samples using a JEOL JES-FA200 spectrometer equipped with an ES-CT470 liquid He variable temperature system, with data recorded and processed using A-System version 1.6.5 PCI J/X-Band and FA-Manager version 1.2.9 V2 series software. Powder X-ray diffraction (pXRD) patterns were recorded at room temperature using with Cu-Kα radiation (λ = 1.54184 Å) on a Rigaku MiniFlex 600 diffractometer. ^{1}H-NMR spectra were obtained using JEOL AL300BX or JEOL AL400SSS spectrometers operating respectively at 300 and 400 MHz and using tetramethylsilane as an internal standard. Proton decoupled ^{13}C-NMR spectra were obtained using JEOL AL300BX or JEOL AL400SSS spectrometers operating respectively at 76 and 101 MHz and using tetramethylsilane as an internal standard. Data was processed on Delta version 5.0.5.1, Always JNM-AL version 6.2, and MestReNova 6.0.2. ^{1}H NMR chemical shifts (δ) were reported in ppm relative to TMS for $CDCl_3$ (δ 0.00) or the residual solvent peak for other solvents. ^{13}C NMR chemical shifts (δ) were reported in ppm relative to the solvent reported. Coupling constants (J) were expressed in Hertz (Hz), shift multiplicities were reported as singlet (s), doublet (d), triplet (t), quartet (q), double doublet (dd), multiplet (m), and broad singlet (bs). High-resolution electrospray ionization time-of-flight mass spectra (ESI-TOF-MS) were measured using a Thermo Scientific Q-Exactive Plus instrument. Tetrakis(3,5-di-t-butyl-4-hydroxyphenyl)porphinatonickel(II) ([T(DtBHP)P]Ni), 2-formyl-5,10,15,20-tetrakis-(3,5-di-t-butyl-4-hydroxyphenyl)porphinatonickel(II)[55] ([T(DtBHP)P]Ni-CHO) and 5,6-bis(4-bromophenyl)pyrazine-2,3-diamine[73] were prepared according to literature methods.

Synthesis: Comprehensive details of the synthesis of receptor molecules are given in the Supporting Information. Briefly for **β-NiOx1** and **β-NiOx3**, **a** round-bottom flask was charged with **4BrPh-Ni(Benzimd)** (400 mg, 62 µmol) dissolved in CH_2Cl_2 (10 mL). 2,3-Dichloro-5,6-dicyano-1,4-benzoquinone (56 mg, 0.25 mmol) was added. The mixture was stirred for 1 h at room temperature with monitoring by thin layer chromatography, then the solvents were removed under reduced pressure, and the solid residue was purified by column chromatography (SiO_2) eluting with CH_2Cl_2, yielding **β-NiOx1** (186 mg, 32% yield) as a dark olive solid. Increasing the polarity of the eluent to 199:1 CH_2Cl_2/methanol mixture provided **β-NiOx3** (210 mg, 28% yield) as a brown solid. **β-NiOx1**: UV/Vis (CH_2Cl_2): λ_{max} (ϵ, $M^{-1}\ cm^{-1}$) = 379 (33 200), 451 (176 000), 552 (16 500), 593 (29 000) nm. ^{1}H NMR (400 MHz, $CDCl_3$): δ 9.64 (s, 1H), 9.42 (d, J = 5.2 Hz, 1H), 8.95 (d, J = 4.8 Hz, 1H), 8.85 (d, J = 5.2 Hz, 1H), 8.81 – 8.76 (m, 3H), 7.84 (s, 2H), 7.77 (d, J = 3.2 Hz, 4H), 7.48 (s, 1H), 7.45 (d, J = 2.8 Hz, 5H), 7.27 (s, 1H), 7.25 (s, 1H), 7.14 (s, 2H), 5.57 (s, 1H), 5.51 (s, 1H), 5.50 (s, 1H), 1.60 (s, 18H), 1.57 (s, 18H), 1.56 (s, 18H), 1.20 (s, 18H). ^{13}C NMR (100.5 MHz, $CDCl_3$): δ 186.2, 154.2, 153.9, 151.4, 149.6, 147.7, 146.2, 145.6, 144.5, 144.3, 144.1, 144.0, 143.3, 142.5, 140.8, 140.1, 139.9, 138.5, 138.0, 135.2, 134.7, 134.5, 134.4, 134.3, 133.6, 133.4, 133.2, 133.1, 132.1, 132.1, 131.5, 131.2, 131.1, 130.9, 125.6, 122.8, 122.7, 122.4, 122.0, 121.3, 108.8, 63.9, 35.5, 34.6, 30.6, 29.3 ppm. FTIR (ATR): ν = 3638 (m), 2956 (s), 2912 (w), 2871 (m), 1724 (w), 1703 (w), 1665 (m), 1644 (m), 1589 (w), 1515 (w), 1485 (m), 1458 (m), 1433 (s), 1389 (m), 1363 (w), 1350 (s), 1312 (m), 1232 (m), 1223 (m), 1196 (s), 1144 (m), 1121 (m), 1072 (m), 1010 (s), 959 (w), 940 (m), 915 (w), 881 (m), 856 (w), 830 (s), 800 (m), 782 (w), 773 (w), 754 (w), 723 (m), 710 (s), 694 (w), 685 (m), 668 (w), 654 (w), 633 (w), 618 (w) cm^{-1}. HRMS: calc'd for $C_{93}H_{99}Br_2N_8NiO_4$: 1608.5538; found: 1608.5464 ([M + H]$^+$).

Specific Surface Area Determinations: Nitrogen adsorption/desorption isotherms were recorded on a BELSORB Max instrument for the estimation of Brunauer–Emmett–Teller (BET) surface area. Samples were loaded into a cell for measurement and heated at 120 °C under reduced pressure for 24 h prior to the collection of the adsorption/desorption isotherms.

X-Ray Crystallography: Crystals of **β-NiOx1** were grown by diffusion of methanol into a solution in chloroform. The single crystal X-ray structure was determined using a Bruker D8 Venture diffractometer with a multi-layered confocal X-ray mirror and MoK_α radiation ($\lambda = 0.71073$ Å) generated at 50 kV and 1.6 mA. Details of data collection and refinement are given in the Supporting Information. Crystallographic data (excluding structure factors) have been deposited with the Cambridge Crystallographic Data Centre with CCDC reference number 2 350 299 (**β-NiOx1**). Copies of the data can be obtained, free of charge, on application to CCDC, 12 Union Road, Cambridge CB2 1EZ, UK http://www.ccdc.cam.ac.uk/perl/catreq/catreq.cgi, e-mail: data_request@ ccdc.cam.ac.uk, or fax: +44 1223 336 033.

Sensor Preparation: Sensing receptor materials were deposited directly onto the four-channel MSS membrane by inkjet deposition using an inkjet spotter (LaboJet-500SP) with a selected nozzle (IJHBS-300) supplied by MICROJET Corporation. Sensor receptor material **β-NiOx1** was dissolved in dimethylsulfoxide (DMSO) at c = 1 mg mL^{-1} for the inkjet deposition. Different numbers of sequential droplet (50-300) depositions were performed. The inkjet stage temperature was set at 70 °C to control the evaporation rate during the deposition process.

Selectivity Tests: Selectivity tests of the inkjet-spotted receptor materials on the MSS chip were performed at ambient temperature using the different VOCs at 20% vapor saturation. Analytes included acids, alcohols, and aldehydes. Ketones and hydrocarbons. Vapors were introduced to the sensor chamber for 30 s using a custom-built setup (Figure 5a) then purged with nitrogen gas for 60 s. Four sampling-purging cycles were performed for each vapor and data were recorded at a sampling rate of 20 Hz by applying a bridge voltage of −0.5 V to the Wheatstone bridge. Here only the 4th cycle was shown and discussed the results accordingly. Sensitivity of the receptor materials to different low-concentration VFAs was performed under an atmosphere saturated with water vapor. To perform different low-concentration (10–500 mM) solutions of acetic acid, propionic acid, and butyric acid in water medium, and measure their headspace concentration to identify the amount of acids in the headspace was prepared. Naturally, this headspace vapor was saturated with water vapor which exactly replicates the ideal condition of the biogas reactor. The headspace acid concentration of the acid solution was also checked by highly sensitive proton-transfer reaction mass spectrometry (PTR-MS) methods as a reference. Several different mixtures of propionic acid and butyric acid with a fixed amount of acetic acid were prepared and measure their headspace concentration to see the variation in MSS signals. Solutions containing a fixed concentration of acetic acid (40 mM) with a range of propionic and butyric acid concentrations (10–200 mM) were prepared in water, and the headspace vapor of the acid mixture was monitored using **β-NiOx1**@MSS. To check the real-time detection limit the MSS saturation intensity was calibrated with the solution concentration of propionic and butyric acid.

Supporting Information

Supporting Information is available from the Wiley Online Library or from the author.

Acknowledgements

The authors are grateful for support by the JST-ERATO Yamauchi Materials Space-Tectonics Project (JPMJER2003), and the Queensland Node of the Australian National Fabrication Facility (ANFF-Q). The authors also thank Japan Society for the Promotion of Science (JSPS) through KAKENHI Grant Nos. JP20H00392 and JP23H05459.

Conflict of Interest

S.M., M.K.C., G.Y., and J.P.H. are inventors on WIPO patent application number WO2023282200A1, submitted by the National Institute for Materials Science (NIMS). J.H., K.N., A.H., K.M., J.L., D.T.P., G.J.R., K.A., Y.Y., and L.K.S. declare no conflict of interest.

Author Contributions

S.M. and J.P.H. designed and initiated the project. J.H. and M.K.C. performed preliminary synthesis and characterization. K.N., A.H, and G.J.H. performed X-ray crystallographic analyses and refinements. D.T.P. undertook spectroscopic characterization of the materials. S.M., K.M., and G.Y. performed and analyzed the sensing properties of the molecules. J.L. modeled the sensing signals elicited from the sensing devices. K.A., Y.Y., and L.K.S. measured and analyzed the textural parameters of the materials. J.P.H. supervised the research, proposed and established the molecular design, and performed the large-scale synthesis of the compounds. S.M. and J.P.H. wrote the manuscript with contributions from all the authors. All authors analyzed the results and contributed to the writing and editing of the manuscript.

Data Availability Statement

The data that support the findings of this study are available in the supplementary material of this article.

Keywords

microporous coordination complex, molecular sensing layer, nanoarchitectonics, nanomechanical device, volatile fatty acid sensor

Received: March 12, 2025
Revised: May 2, 2025
Published online: May 28, 2025

---

[1] Global Potential of Biogas, http://www.worldbiogasassociation.org/global-potential-of-biogas/ (accessed: July 2019).
[2] A. Costa, C. Ely, M. Pennington, S. Rock, C. Staniec, J. Turgeon, Anaerobic Digestion and its Applications, Environmental Protection Agency Bulletin, **2015** (EPA/600/R-15/304), United States.
[3] M. Zamanzadeh, L. H. Hagen, K. Svensson, R. Linjordet, S. J. Horn, *Sci. Rep.* **2017**, *7*, 17664.
[4] E. D. Erickson, P. A. Tominac, V. M. Zavala, *Nat. Sustain.* **2023**, *6*, 438.
[5] J. N. Meegoda, B. Li, K. Patel, L. B. Wang, *Int. J. Environ. Res. Public Health* **2018**, *15*, 2224.
[6] M. Madsen, J. B. Holm-Nielsen, K. H. Esbensen, *Renewable Sustainable Energy Rev.* **2011**, *15*, 3141.
[7] M. A. Khan, H. H. Ngo, W. S. Guo, Y. Liu, L. D. Nghiem, F. I. Hai, L. J. Deng, J. Wang, Y. Wu, *Bioresour. Technol.* **2016**, *219*, 738.
[8] A. J. Ward, P. J. Hobbs, P. J. Holliman, D. L. Jones, *Bioresour. Technol.* **2008**, *99*, 7928.
[9] D. Li, L. Chen, X. Liu, Z. Mei, H. Ren, Q. Cao, Z. Yan, *Bioresour. Technol.* **2017**, *245*, 90.
[10] L. Li, Q. He, Y. Wei, Q. He, X. Peng, *Bioresour. Technol.* **2014**, *171*, 491.

[11] X. Goux, M. Calusinska, S. Lemaigre, M. Marynowska, M. Klocke, T. Udelhoven, E. Benizri, P. Delfosse, *Biotechnol. Biofuels* **2015**, *8*, 122.

[12] J. A. Magdalena, S. Greses, C. González-Fernández, *Sci. Rep.* **2019**, *9*, 18374.

[13] T. B. Ferreira, F. Passos, C. A. L. Chernicharo, C. L. de Souza, *Waste Biomass Valorization* **2021**, *12*, 4407.

[14] X. Li, X. Jin, N. Zhao, I. Angelidaki, Y. Zhang, *Water Res.* **2017**, *119*, 67.

[15] H. Sun, S. Wu, R. Dong, *Chem. Eng. Technol.* **2016**, *39*, 599.

[16] A. Schievano, A. Colombo, A. Cossettini, A. Goglio, V. D'Ardes, S. Trasatti, P. Cristiani, *Waste Manage.* **2017**, *71*, 785.

[17] X. Jin, I. Angelidaki, Y. Zhang, *Environ. Sci. Technol.* **2016**, *50*, 4422.

[18] Y. Chen, X. Zhang, Y. Chen, *Bioresou. Technol.* **2021**, *339*, 125569.

[19] S. K. Bhatia, Y.-H. Yang, *Rev. Environ. Sci. Biotechnol.* **2017**, *16*, 327.

[20] R. Fernández, R. M. Dinsdale, A. J. Guwy, G. C. Premier, *Crit. Rev. Environ. Sci. Technol.* **2015**, *46*, 209.

[21] R. J. Fussell, D. V. McCalley, *Analyst* **1987**, *112*, 1213.

[22] H. Q. Yu, H. H. P. Fang, *Water Res.* **2003**, *37*, 55.

[23] A. Akhtar, S. Sadaf, R. Zhou, Q. Ling, S. Luo, M. Han, W. Di, J. Liu, D. Chen, X. Chu, *J. Alloys Compd.* **2025**, *1010*, 177715.

[24] N. J. Pineau, F. Krumeich, A. T. Güntner, S. E. Pratsinis, *Sens. Actuators, B* **2021**, *327*, 128843.

[25] C. Bücher, J. Burtscher, K. J. Domig, *Compr. Rev. Food Sci. Food Saf.* **2021**, *20*, 4299.

[26] T. W. Chao, C. J. Liu, A. H. Hsieh, H. M. Chang, Y. S. Huang, D. S. Tar, *Sens. Actuators, B* **2007**, *122*, 95.

[27] C. Wuthrich, Z. Fan, G. Vergeres, F. Wahl, R. Zenobi, S. Giannoukos, *Anal. Methods* **2023**, *15*, 553.

[28] Y.-C. Wang, Z.-S. Sun, S.-Z. Wang, S.-Y. Wang, S.-X. Cai, X.-Y. Huang, K. Li, Z.-T. Chi, S.-D. Pan, W.-F. Xie, *J. Mater. Sci.* **2019**, *54*, 14055.

[29] W.-F. Fu, H.-M. Zhang, X.-B. Li, Y.-W. Xing, Y.-X. Guo, Y.-Y. Feng, Y.-J. Li, S.-Q. Han, K.-F. Ma, H.-H. Cao, S.-N. Liu, X.-M. Jia, C.-H. Zhou, *J. Mater. Sci.: Mater. Electron.* **2023**, *34*, 1560.

[30] G. Li, Y. Su, Y.-Y. Li, Y.-X. Li, Z. Guo, X.-J. Huang, J.-H. Liu, *Nanotechnology* **2018**, *29*, 445501.

[31] V. Platonov, M. Rumyantseva, *Sensors and Actuators B: Chemical* **2025**, *433*, 137535.

[32] Z.-K. Chen, S.-C. Ng, S. F. Y. Li, L. Xu, H. S. O. Chan, *Synth. Met.* **1997**, *87*, 201.

[33] N. G. Torad, H. El-Hosainy, M. Esmat, K. E. El-Kelany, R. Tahawy, J. Na, Y. Ide, N. Fukata, W. Chaikittislip, J. P. Hill, X. Zhang, M. El-Kemary, Y. Yamauchi, *ACS Appl. Mater. Interfaces* **2021**, *13*, 48595.

[34] G. Adam, S. Lemaigre, X. Goux, P. Dekfosse, A.-C. Romain, *Bioresour. Technol.* **2015**, *178*, 285.

[35] L. Kosinski, P. A. Engen, B. Swanson, M. Villanueva, M. Shaijh, S. J. Green, A. Naqib, B. Hamaker, T. M. Cantu-Jungles, A. Keshavarzian, *Sensors* **2025**, *25*, 797.

[36] W. Ling, S. Zhang, S. Cao, Y. Pu, D. Zhu, *Sens. Actuators, B* **2023**, *377*, 133057.

[37] S. A. Zakaria, M. H. Amini, S. H. Ahmadi, *ACS Omega* **2023**, *8*, 23613.

[38] P. Papa, E. Zampetti, F. N. Molinari, F. De Cesare, C. Di Natale, G. Tranfo, A. Macagnano, *Sensors* **2024**, *24*, 2174.

[39] H. Sun, M. Xu, S. Wu, R. Dong, I. Angelidaki, Y. Zhang, *Chemosphere* **2021**, *273*, 129660.

[40] A. Yavarinasab, S. Flibotte, S. Liu, C. Tropini, *Sens. Actuators, B* **2023**, *393*, 134182.

[41] L. Cheng, S. Y. Ma, T. T. Wang, J. Luo, X. B. Li, W. Q. Li, Y. Z. Mao, D. J. Gz, *Mater. Lett.* **2014**, *137*, 265.

[42] E. S. Tillman, M. E. Koscho, R. H. Grubbs, N. S. Lewis, *Anal. Chem.* **2003**, *75*, 1748.

[43] C. Liu, L. Shang, H. Yoshioka, B. Chen, K. Hayashi, *Anal. Chim. Acta* **2018**, *1010*, 1.

[44] L. Vergelli, F. Frasca, C. Bertolin, G. Favero, A. M. Siani, *Environ. Pollut.* **2025**, *368*, 125829.

[45] Y. Sun, H. Xu, L. Wang, C. Yu, J. Zhou, Q. Chen, G. Sun, W. Huang, *J. Mater. Chem. B* **2021**, *9*, 983.

[46] H. L. Ritter, J. H. Simons, *J. Am. Chem. Soc.* **1945**, *67*, 757.

[47] B. Xu, P. Zhang, J. Zhu, Z. Liu, A. Eichler, X.-Q. Zheng, J. Lee, A. Dash, S. More, S. Wu, Y. Wang, H. Jia, A. Naik, A. Bachtold, R. Yang, P. X.-L. Feng, Z. Wang, *ACS Nano* **2022**, *16*, 15545.

[48] F. Fogliano, B. Besga, A. Reigue, L. M. de Lépinay, P. Heringlake, C. Gouriou, E. Eyraud, W. Wernsdorfer, B. Pigeau, O. Arcizet, *Nat. Commun.* **2021**, *12*, 4124.

[49] J. Chaste, A. Eichler, J. Moser, G. Ceballos, R. Rurali, A. Bachtold, *Nat. Nanotechnol.* **2012**, *7*, 301.

[50] G. Yoshikawa, T. Akiyama, S. Gautsch, P. Vettiger, H. Rohrer, *Nano Lett.* **2011**, *11*, 1044.

[51] I. Osica, A. F. A. A. Melo, F. C. D. A. Lima, K. Shiba, G. Imamura, F. N. Crespilho, J. Betlej, K. J. Kurzydowski, G. Yoshikawa, K. Ariga, *ACS Appl. Nano Mater.* **2020**, *3*, 4061.

[52] K. Minami, G. Imamura, R. Tamura, K. Shiba, G. Yoshikawa, *Biosensors* **2022**, *12*, 762.

[53] G. Imamura, K. Shiba, G. Yoshikawa, T. Washio, *Sci. Rep.* **2019**, *9*, 9768.

[54] K. Minami, H. Kobayashi, M. Matoba, Y. Kamiya, S. Maji, T. Nemoto, M. Tohno, R. Nakakubo, G. Yoshikawa, *Biosensors* **2023**, *13*, 152.

[55] M. K. Chahal, S. Maji, A. Liyanage, Y. Matsushita, P. Tozman, D. T. Payne, W. Jevasuwan, N. Fukata, P. A. Karr, J. Labuta, L. K. Shrestha, S. Ishihara, K. Ariga, F. D'Souza, G. Yoshikawa, Y. Yamauchi, J. P. Hill, *Mater. Chem. Front.* **2023**, *7*, 325.

[56] Y. Zhu, X. Dong, J. Cheng, L. Wang, C. Zhao, Y. Deng, S. Xie, Y. Pan, Y. Zhao, G. Sun, T. Ni, *Chin. Chem. Lett.* **2023**, *34*, 107930.

[57] R. Paolesse, S. Nardis, D. Monti, M. Stefanelli, C. Di Natale, *Chem. Rev.* **2016**, *117*, 2517.

[58] Q. Li, M. Xuan, A. Wang, Y. Jia, S. Bai, X. Yan, J. Li, *Matter* **2022**, *5*, 3643.

[59] X. Song, Y. Wang, C. Wang, D. Wang, G. Zhuang, K. O. Kirlikovali, P. Li, O. K. Farha, *J. Am. Chem. Soc.* **2022**, *144*, 10663.

[60] Y. Yang, L. Li, R.-B. Lin, Y. Ye, Z. I. Yao, L. Yang, F. Xiang, S. Chen, Z. Zhang, S. Xiang, B. Chen, *Nat. Chem.* **2021**, *13*, 933.

[61] H. Sun, K. Xiao, Z. Zeng, B. Yang, H. Duan, H. Zhao, Y. Zhang, *Chem. Eng. J.* **2022**, *449*, 137833.

[62] A. J. Fletcher, E. J. Cussen, D. Bradshaw, M. J. Rosseinsky, K. M. Thomas, *J. Am. Chem. Soc.* **2004**, *126*, 9750.

[63] X. Fan, J. Zhou, T. Wang, J. Zheng, X. Li, *RSC Adv.* **2015**, *5*, 58595.

[64] K. Minami, K. Shiba, G. Yoshikawa, *J. Appl. Phys.* **2021**, *129*, 124503.

[65] J. Sun, L. Zhang, K. C. Loh, *Bioresources Bioprocess.* **2021**, *8*, 68.

[66] J. Zou, G. Li, D. Zheng, Y. Wang, C. Feng, Y. Sun, M. Juan, X. Bai, M. Wu, *ACS Sustainable Chem. Eng.* **2021**, *9*, 12540.

[67] X. Cui, H. Sun, M. Sobhi, X. Ju, J. Guo, R. Dong, *ACS Sustainable Chem. Eng.* **2020**, *8*, 6713.

[68] C. Bruni, A. Foglia, A. L. Eusebi, N. Frison, Ç. Akyol, F. Fatone, *ACS Sustainable Chem. Eng.* **2021**, *9*, 9970.

[69] J. Slavin, *Nutrients* **2013**, *5*, 1417.

[70] C. Xie, C. Qi, J. Zhang, W. Wang, X. Meng, A. Aikepaer, Y. Lin, C. Su, Y. Liu, X. Feng, H. Gao, *Biochem. Pharmacol.* **2025**, *233*, 116791.

[71] B. Thulasinathan, K. N. Suvilesh, S. Maram, E. Grossmann, Y. Ghouri, E. P. Teixeiro, J. Chan, J. T. Kaifi, S. Rachagani, *Gut Microbes* **2025**, *17*, 2483780.

[72] Y. Chen, C.-T. Ho, X. Zhang, *J. Food. Sci.* **2025**, *90*, 70132.

[73] N. Sato, H. Mizuno, *J. Chem. Res.* **1997**, *7*, 250.